C. T.-C. Nguyen, "Frequency-selective MEMS for miniaturized communication devices (invited)," *Proceedings*, 1998 IEEE Aerospace Conference, vol. 1, Snowmass, Colorado, March 21-28, 1998, pp. 445-460.

Frequency-Selective MEMS for Miniaturized Communication Devices

Clark T.-C. Nguyen
Center for Integrated Sensors and Circuits
Department of Electrical Engineering and Computer Science
University of Michigan
2406 EECS Bldg., 1301 Beal Ave., Ann Arbor, Michigan 48109-2122, email: ctnguyen@eecs.umich.edu

Abstract—With *Q*'s in the tens to hundreds of thousands, micromachined vibrating resonators are proposed as IC-compatible tanks for use in the low phase noise oscillators and highly selective filters of communications subsystems. To date, LF oscillators have been fully integrated using merged CMOS+microstructure technologies, and bandpass filters consisting of spring-coupled micromechanical resonators have been demonstrated in the HF range. In particular, two-resonator micromechanical bandpass filters have been demonstrated with frequencies up to 14.5 MHz, percent bandwidths on the order of 0.2%, and insertion losses less than 1 dB. Higher-order three-resonator filters with frequencies near 455 kHz have also been achieved, with equally impressive insertion losses for 0.09% bandwidths, and with more than 64 dB of passband rejection. Evidence suggests that the ultimate frequency range of this high-*Q* tank technology depends upon material limitations, as well as design constraints—in particular, to the degree of electromechanical coupling achievable in micro-scale resonators.

TABLE OF CONTENTS

1. INTRODUCTION

Vibrating mechanical tank components, such as crystal and SAW resonators, are widely used for frequency selection in communication subsystems because of their high quality factor (*Q*'s in the tens of thousands) and exceptional stability against thermal variations and aging. In particular, the majority of heterodyning communication transceivers rely heavily upon the high *Q* of SAW and bulk acoustic mechanical resonators to achieve adequate frequency selection in their RF and IF filtering stages and to realize the required low phase noise and high stability in their local oscillators. At present, such mechanical resonator tanks are off-chip components, and so must interface with integrated electronics at the board level, often consuming a sizable portion of the total subsystem area. In this respect, these devices pose an important bottleneck against the ultimate miniaturization and portability of wireless transceivers. For this reason, many research efforts are focused upon strategies for either miniaturizing these components [1-5] or eliminating the need for them altogether [6,7].

Recent demonstrations of micro-scale high-*Q* oscillators and mechanical bandpass filters with area dimensions on the order of 30 μm × 20 μm now bring the first of the above strategies closer to reality. Such devices utilize high-*Q*, on-chip, micromechanical (abbreviated "μmechanical") resonators [8,9] constructed in polycrystalline silicon using IC-compatible surface micromachining fabrication techniques, and featuring *Q*'s of over 80,000 [10] under vacuum and center frequency temperature coefficients in the range of -10 ppm/^{0}C (several times less with nulling techniques) [11]. To date, two-resonator micromechanical bandpass filters have been demonstrated with frequencies up to 14.5 MHz, percent bandwidths on the order of 0.2%, and insertion losses less than 1 dB [12-15]. Higher-order three-resonator filters with frequencies near 455 kHz have also been achieved, with equally impressive insertion losses for 0.09% bandwidths, and with more than 64 dB of passband rejection [16]. LF (i.e., 20 kHz), high-*Q* oscillators, fully-integrated with sustaining CMOS electronics, have also been demonstrated in this technology [17-19].

For use in many portable communications applications, however, higher frequencies must be achieved. Thus, frequency extension into the higher VHF and UHF ranges is presently the subject of ongoing research. This paper presents an overview of recent advances in frequency-selective MEMS devices aimed at both size reduction and performance enhancement of transceivers via miniaturization of high-*Q* signal processing elements. Specific results will be reported, including a review of integrated oscillator work and of recently demonstrated micromechanical resonators and filters in the HF range. The remainder of this paper then focuses upon projections for the ultimate frequency range and performance of these communications devices.

2. ADVANTAGES OF MEMS

Reduced size constitutes the most obvious incentive for replacing SAWs and crystals by equivalent μmechanical devices. The substantial size difference between micromechanical resonators and their macroscopic counterparts is illustrated in Fig. 1, which compares a typical SAW resonator with a clamped-clamped beam micromechanical resonator of comparable frequency. The particular μresonator shown is excited electrostatically via parallel-plate capacitive transducers and designed to vibrate in a direction parallel to the substrate with a frequency determined by material properties, geometric dimensions, and stress in the material. Typical

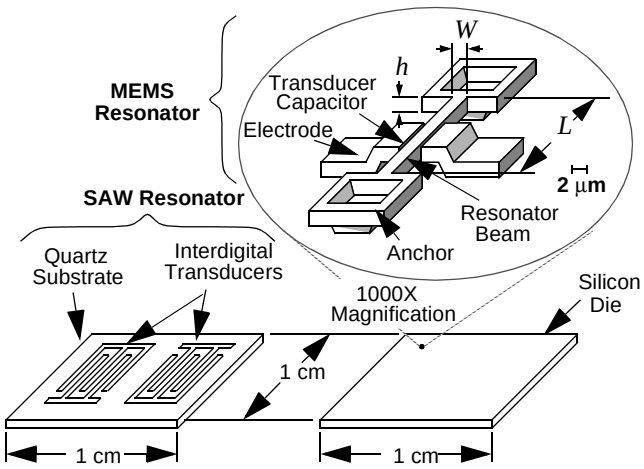

Fig. 1: Size comparison between present-day SAW resonator technology and the described high-*Q* μmechanical resonator technology.

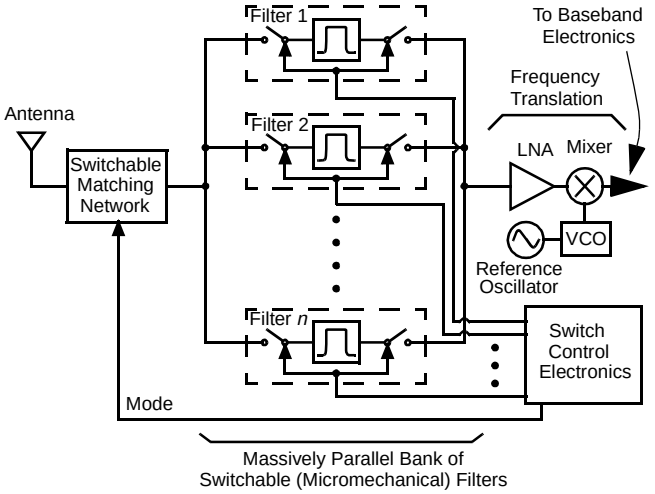

Fig. 2: Possible front-end receiver architecture utilizing a parallel bank of switchable micromechanical filters for a first stage of channel selection. Note that it is also possible to replace the frequency translation blocks with a low clock-rate sub-sampling down-converter.

dimensions for a 100 MHz micromechanical resonator are $L \approx 12.9$ μm, $W=2$ μm, and $h=2$ μm. With electrodes and anchors, this device occupies an area of 420 μm^2 = 0.00042 mm^2. Compared with the several mm^2 required for a typical VHF range SAW resonator, this represents several orders of magnitude in size reduction.

A related incentive for the use of micromechanics is integrability. Micromechanical structures can be fabricated using the same planar process technologies used to manufacture integrated circuits. Several technologies demonstrating the merging of CMOS with surface micromachining have emerged in recent years [18,20,21], and one of these is now used for high volume production of commercial accelerometers [20]. Using similar technologies, complete systems containing integrated micromechanical filters and oscillator tanks, as well as sustaining and amplification electronics, all on a single chip, are possible. This in turn makes possible high-performance, single-chip transceivers, with heterodyning architectures and all the communication link advantages associated with them. Other advantages inherent with integration are also obtained, such as elimination of board-level parasitics that could otherwise limit filter rejections and distort their passbands.

MEMS Components for Transceivers

The front-end of a wireless transceiver typically contains a good number of off-chip, high-*Q* components that are potentially replaceable by micromechanical versions. Among the components targeted for replacement are RF filters, including image rejection filters, with center frequencies ranging from 800 MHz to 2.5 GHz; IF filters, with center frequencies ranging from 455 kHz to 254 MHz; and high-*Q*, low phase noise local oscillators, with frequency requirements in the 10 MHz to 2.5 GHz range.

For the specific case of sub-sampling transceiver architectures, a tunable high-*Q* filter up at RF frequencies is highly desirable, since it would enable direct down-conversion of RF signals to baseband using a low-rate (hence, low power) sub-sampling analog-to-digital converter [7]. Partially due to their own high stability, high-*Q* filters are generally very difficult to tune over large frequency ranges, and MEMS-based filters are no exception to this. Although μmechanical resonators can be tuned over larger frequency ranges than other high-*Q* tank technologies, with voltage-controllable tuning ranges of up to 5% depending on design, a single micromechanical filter still lacks the tuning range needed for some wide-band applications.

Thanks to the tiny size of micromechanical filters, however, there no longer needs to be only one filter. One of the major advantages of micromechanical filters is that, because of their tiny size and zero dc power dissipation, many of them (perhaps hundreds or thousands) can be fabricated onto a smaller area than occupied by a single one of today's macroscopic filters. Thus, rather than use a single tunable filter to select one of several channels over a large frequency range, a massively parallel bank of switchable, micromechanical filters can be utilized, in which desired frequency bands can be switched in, as needed. The simplified block diagram for such a front-end architecture is illustrated in Fig. 2, where each filter switch combination corresponds to a single micromechanical filter, with input and output switches activated by the mere application or removal of dc-bias voltages (V_P, in later discussions) from the resonator elements. By further exploiting the switching flexibility of such a system, some very resilient frequency-hopping spread spectrum transceiver architectures can be envisioned that take advantage of simultaneous switching of high-*Q* micromechanical filters and oscillators.

The next sections now focus upon the subject micromechanical resonator devices.

3. Micromechanical Resonator Oscillators

The scanning electron micrograph (SEM) for a 16.5 kHz micromechanical resonator oscillator, fully integrated with sustaining CMOS electronics, is shown in Fig. 3 [19]. To maximize frequency stability against supply voltage variations [17], a folded-beam, comb-transduced micromechanical resonator is utilized [8]. As shown, this μresonator consists of a finger-supporting shuttle mass suspended 2 μm

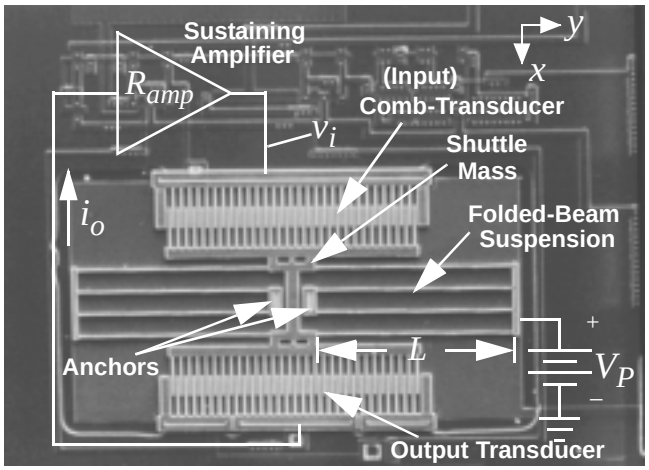

Fig. 3: SEM of a 16.5 kHz CMOS μresonator oscillator with schematics explicitly depicting circuit topology. The μresonator occupies 420×230 μm^2

above the substrate by folded flexures, which are anchored to the substrate at two central points. The shuttle mass is free to move in the *x*-direction indicated, parallel to the plane of the silicon substrate, with a fundamental resonance frequency determined largely by material properties and by geometry, given by the expression [8]

$$f_o = \frac{1}{2\pi}\left[\frac{2Eh(W/L)^3}{\left(M_P + \frac{1}{4}M_t + \frac{12}{35}M_b\right)}\right]^{1/2}, \qquad (1)$$

where E is the Young's modulus of the structural material, M_P is the shuttle mass, M_t is the mass of the folding trusses, M_b is the total mass of the suspending beams, W and h are the cross-sectional width and thickness, respectively, of the suspending beams, and L is indicated in Fig. 3.

To properly excite this device, a voltage consisting of a dc-bias V_P and an ac excitation v_i is applied across one of the resonator-to-electrode comb-capacitors (i.e., the input transducer). This creates a force component between the electrode and resonator proportional to the product $V_P v_i$ and at the frequency of v_i. When the frequency of v_i nears its resonance frequency, the μresonator begins to vibrate, creating a dc-biased time-varying capacitor $C_o(x,t)$ at the output transducer. A current given by

$$i_o = V_P \frac{\partial C_o}{\partial x}\frac{\partial x}{\partial t} \qquad (2)$$

is then generated through the output transducer and serves as the output of this device. When plotted against the frequency of the excitation signal v_i, the output current i_o traces out the bandpass biquad characteristic expected for a high-Q tank circuit. Figure 4 presents the transconductance spectrum for the micromechanical resonator of Fig. 3, measured under 20 mTorr vacuum using a dc-bias V_P of 20 V and an excitation signal of 1 mV peak. From this plot, the extracted Q is about 50,000.

Note also from the discussion associated with (2) that the effective input force ($\sim V_P v_i$) and output current can be nulled by setting V_P=0V. Thus, a micromechanical resonator (or filter constructed of such resonators) can be switched in and out by the mere application and removal of the dc-bias voltage V_P. As described in conjunction with Fig. 2, such switchability can be used to great advantage in receiver architectures.

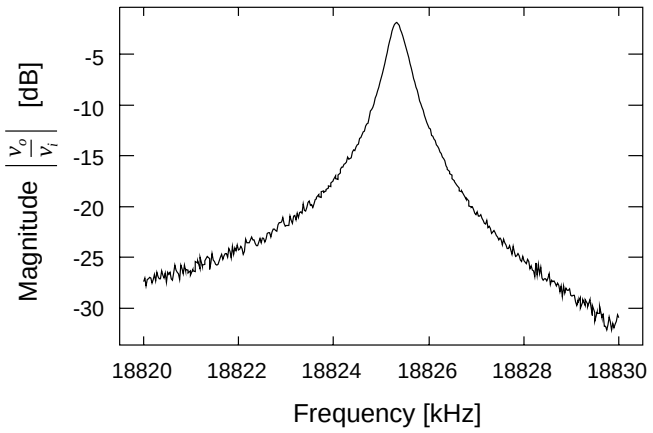

Fig. 4: Measured transconductance spectrum for a folded-beam, capacitive-comb transduced polysilicon μmechanical resonator operated under a vacuum pressure of 20 mTorr.

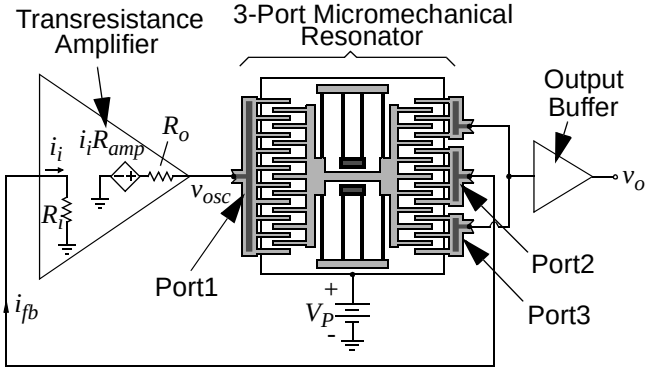

Fig. 5: System level schematic for the μresonator oscillator of Fig. 3.

Oscillator Design

A system-level schematic for the oscillator of Fig. 3 is shown in Fig. 5. As shown, this oscillator utilizes a three-port μmechanical resonator, for which two ports are embedded in a (zero phase shift) positive feedback loop in series with a sustaining transresistance amplifier, while a third port is directed to an output buffer. The use of a third port effectively isolates the sustaining feedback loop from variations in output loading.

For the purposes of start-up design, a small-signal equivalent circuit for the micromechanical resonator is useful. The small-signal equivalent circuit for the three-port micromechanical resonator of Fig. 5, obtained via an appropriate impedance analysis [17], is presented in Fig. 6, along with equations for each of the elements. As shown, the electrical impedances looking into each of the ports are modelled by LCR tanks in parallel with shunt capacitors C_{on}, while port-to-port coupling is modeled via current-controlled current sources. Details of the overall design and small-signal circuit model for the three-port μresonator of Fig. 3 are summarized in Tables 1 and 2.

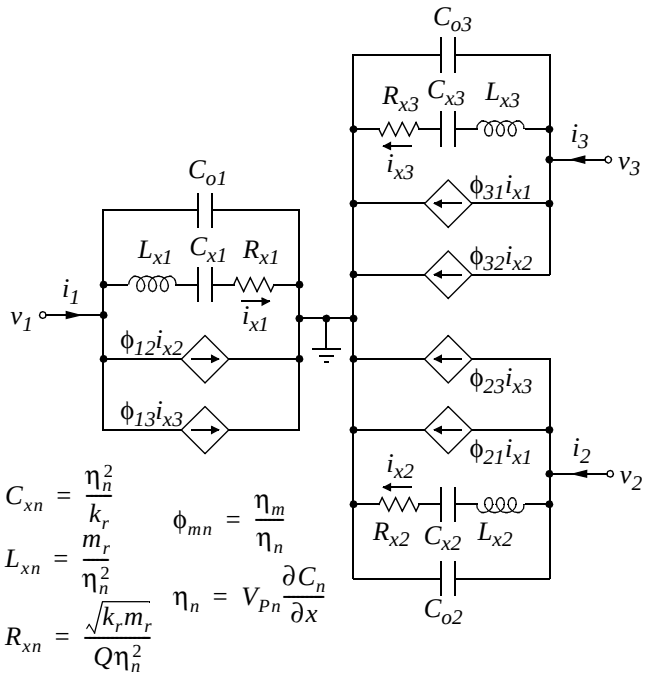

Fig. 6: Small-signal equivalent circuit for a three-port μmechanical resonator with equations for the elements. In the equations, m_r is the effective mass of the resonator at the shuttle location, k_r is the corresponding system spring constant, and $\partial C_n/\partial x$ is the change in capacitance per unit displacement at port n.

Table 1: μMechanical Resonator Data

Parameter	Value	Units
Folded-Beam Length, L	185.3	μm
Folded-Beam Width, W	1.9	μm
Structural Layer Thickness, h	2	μm
Effective Mass, m_r	5.73×10^{-11}	kg
System Spring Constant, k_r	0.65	N/m
No. Finger Overlaps at Port 1, N_{g1}	60	—
No. Finger Overlaps at Port 2, N_{g2}	30	—
No. Finger Overlaps at Port 3, N_{g3}	30	—
Finger Gap Spacing, d	2	μm
Finger Overlap Length, L_d	20	μm
$\partial C/\partial x$ per Finger Overlap	1.06×10^{-11}	F/m
Measured Q at 20 mTorr	23,400	—
Young's Modulus, E [8]	150	GPa
Density of Polysilicon, ρ	2300	kg/m^3
Calculated Resonance Frequency, f_o	16.9	kHz
Measured Resonance Frequency, f_o	16.5	kHz

Table 2: μResonator Equivalent Circuit Element Values*

Element	Port 1 (n=1)	Port 2 (n=2)	Port 3 (n=3)	Units
C_{on}	11.7	5.8	5.8	fF
C_{xn}	0.65	0.16	0.16	fF
L_{xn}	136.5	545.8	545.8	kH
R_{xn}	620.8	2483.1	2483.1	kΩ
ϕ_{mn}	$\phi_{12} = -2$	$\phi_{21} = -0.5$	$\phi_{41} = -0.5$	A/A
	$\phi_{14} = -2$	$\phi_{24} = 1$	$\phi_{42} = 1$	A/A

* Calculated using values in Table 1 and V_{Pn}=35V.

Assuming that the bandwidth of the sustaining transresistance amplifier is much larger than the oscillation frequency (so as to prevent excess phase shift at that frequency), oscillation start-up will occur when the loop gain A_l is larger than unity. For this series resonant oscillator design, the loop gain is given by

$$A_l = \frac{R_{amp}}{R_{x12} + R_i + R_o}, \tag{3}$$

where R_i is the input resistance of the transresistance amplifier, R_o is its output resistance, R_{amp} is its transresistance gain, and R_{x12} is the equivalent series motional resistance between ports 1 and 2 of the μmechanical resonator, given by [17]

$$R_{x12} = -\frac{v_1}{i_2} = -\frac{R_{x1}}{\phi_{21}} = \frac{R_{x1}}{|\phi_{21}|}, \tag{4}$$

where variables are defined in Fig. 6.

Conceptually, this oscillator may also be modelled as a negative resistance oscillator, with the quantities ($-R_{amp}$) and (R_{x12}+R_i+R_o) comprising negative and positive resistances, respectively. During start-up, if A_l>1, the negative (trans)resistance of the amplifier R_{amp} is larger in magnitude than the positive resistance (R_{x12}+R_i+R_o), and oscillation results. Oscillation builds up until either some form of nonlinearity or a designed automatic-level control circuit alters either or both resistors so that, R_{amp}=R_{x12}+R_i+R_o, at which point A_l=1 and the oscillation amplitude limits. Unlike many of its macroscopic counterparts, amplitude limiting of this oscillator ultimately arises from nonlinearity in the micromechanical resonator [17].

The transresistance sustaining amplifier in Fig. 3 utilizes a linear region MOS resistor in a shunt-shunt feedback configuration around an NMOS driver device to implement a gate voltage-controllable transresistance gain [17,19]. Using a 2 μm-channel length CMOS technology, the circuit achieves a bandwidth of 12.7 MHz when biased for a transresistance gain of 5.5 MΩ—sufficient gain and bandwidth to achieve zero-phase-shift oscillation when coupled with the μresonator of Tables 1 and 2. The output circuit is a replica of the sustaining amplifier with added buffer electronics for driving off-chip loads. Circuit details for both amplifiers can be found in [17]. The total area consumed by the 16.5 kHz pro-

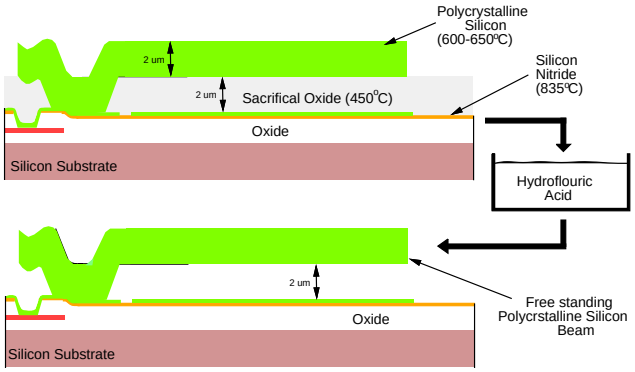

Fig. 7: Cross-sections depicting the fabrication sequence used to achieve the micromechanical filter. (a) Required film layers up to the release etch step. (b) Resulting free-standing beam following a release etch in hydroflouric acid.

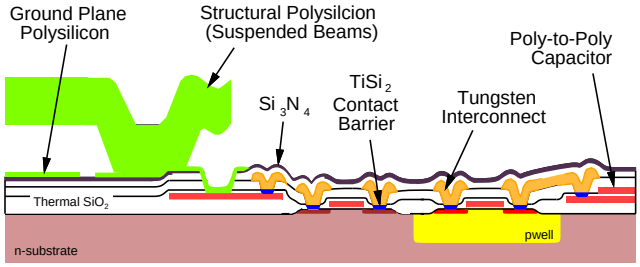

Fig. 8: Final cross-section of the CMOS plus microstructures process used to realize the fully integrated oscillator of Fig. 3.

totype oscillator of Fig. 3 is $420 \times 330\ \mu m^2$. As will become apparent, higher frequency oscillators will require μresonators with much less mass, and thus, should occupy an even smaller area.

Fully-Integrated Oscillator Fabrication

Surface Micromachining—A polysilicon surface micromachining technology [8,9] was used to fabricate the μmechanical resonator of this work. In this process, a series of film depositions and lithographic patterning steps—identical to similar steps used in planar fabrication technologies—are utilized to first achieve the cross-section shown in Fig. 7(a). Here, a sacrificial oxide layer supports the structural polysilicon material during deposition, patterning, and subsequent annealing. In the final step of the process, the wafer containing cross-sections similar to Fig. 7(a) is dipped into a solution of hydroflouric acid, which etches away the sacrificial oxide layer without significantly attacking the polysilicon structural material. This leaves the free-standing structure shown in Fig. 7(b), capable of movement in three dimensions, if necessary.

Merging CMOS With Micromechanics—The technology for the fully monolithic high-*Q* oscillator of Fig. 3 combines planar CMOS processing with surface micromachining to achieve the cross-section shown in Fig. 8 [18,22]. The technologies are combined in a modular fashion, in which the CMOS processing and surface micromachining are done in separate process modules, with no intermixing of CMOS or micromachining steps. This **M**odular **I**ntegration of **C**MOS and micro**S**tructures (MICS) process has the advantage in that it allows the use of nearly any CMOS process with a variety of surface micromachining processes.

In order to avoid problems with microstructure topography, which commonly includes step heights of 2 to 3 μm, the CMOS module is fabricated before the microstructure module. Although this solves topography problems, it introduces constraints on the CMOS. Specifically, the metallization and contacts for the electronics must be able to survive post-CMOS micromachining processing with temperatures up to 835°C. Aluminum interconnect, the industry standard, cannot survive these temperatures. For this reason, tungsten with $TiSi_2$ contact barriers is used as interconnect for this process.

Unfortunately, the use of tungsten for circuit interconnect is not consistent with mainstream IC technologies, where aluminum interconnect predominates. Given that IC manufacturers have already invested enormous resources into the development of multi-level aluminum interconnect technologies, and further given the inferior resistivity of tungsten versus aluminum, the described tungsten-based post-CMOS process, although useful as a demonstration tool, is not likely to flourish in industry. Rather, other processes which intermix CMOS and micromachining fabrication steps [20] or which fabricate micromechanics before circuits (i.e., pre-circuit processes) [21] have become more prevalent. These processes, however, have their own associated limitations: mixed processes often require longer, more expensive development periods for new product lines; while pre-circuit processes may place limitations on foundry-based fabrication schemes, since circuit foundries may be sensitive to contamination from MEMS foundries. Thus, research aimed at achieving a truly modular merged circuits+microstructures technology is ongoing.

Oscillator Performance

As seen from Table 2, resonator dc-bias voltages on the order of 40V were required to obtain equivalent circuit R_x's in the range of hundreds of kΩ's for this early micromechanical resonator design. As will be seen, more recent μmechanical resonator designs used in bandpass filters allow much smaller operation voltages and can achieve much smaller values of motional resistance R_x (on the order of several ohms). Nevertheless, using V_P's in the range of 40V and circuit supplies of 5V, the oscillator of Fig. 3 was successfully operated and tested [17]. Oscillations were observed both electronically and visually under a microscope.

At present (to the author's knowledge), commercial phase noise measurement instrumentation is not available in the 16.5 kHz frequency range of this oscillator. Attempts to measure the phase noise using a custom-built measurement system were unsuccessful, as the noise floor of the custom-built unit was higher than the apparent phase noise of the actual oscillator. However, one can still deduce that the μmechanical resonator oscillator performs at least as well as the measurement unit, which already shows a noise floor indicative of high-*Q* oscillator performance. Low phase noise performance is further verified by comparison of the μmechanical resonator's output with that of high quality instrumentation oscillators using an HP3561A Dynamic Signal Analyzer. For selected values of resonator dc-bias V_P, the output spectrum of the 16.5 kHz CMOS micromechanical resonator oscillator

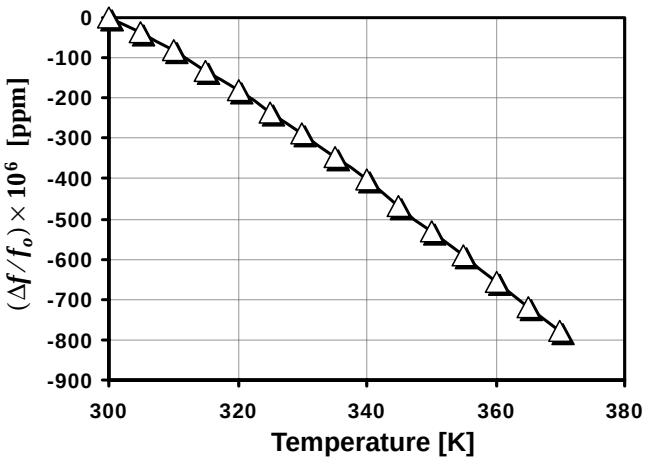

Fig. 9: Measured plot of fractional frequency change $\Delta f/f$ versus temperature for a folded-beam, capacitive-comb transduced polysilicon μmechanical resonator. (Frequency measurements were made under small-amplitude, linear conditions for this plot—i.e., V_P=20V and v_i=1 mV.)

prototype had a spectral purity (as seen by the close to carrier noise roll-off) between that of an HP 3314A Function Generator (synthesized output, i.e. phase-locked VCO) and the source of an HP 4195A Network Analyzer (high quality) [17].

Thermal Stability—Due to the extremely high-*Q* of the μmechanical resonator tank, the thermal stability of the overall oscillator is somewhat independent of the sustaining amplifier circuit, and depends primarily on the temperature dependence of the μmechanical resonator. Figure 9 shows a measured plot of fractional frequency change $\Delta f/f$ versus temperature for a folded-beam, capacitive-comb transduced polysilicon μmechanical resonator fabricated using the surface micromachining process described above. From the slope of the curve, the temperature coefficient of the resonance frequency, TC_{fr}, for this device is –10 ppm/°C. Through manipulation of Eq. (1), the temperature coefficient of the Young's modulus, TC_E, may be expressed as

$$TC_E = 2TC_{fr} - TC_h \ . \qquad (5)$$

Using the measured value of TC_{fr} = –10 ppm/°C, (5) yields TC_E = –22.5 ppm/°C. This value is considerably smaller than a previously reported number of -74.5 ppm/°C [23], and it is stated tentatively pending a more systematic study of other factors which can affect the TC_{fr}.

The measured TC_{fr} of –10 ppm/°C can be reduced further via on-chip compensation or on-chip oven control techniques. Such integrated oven control has been demonstrated that reduced the TC_{fr} of a capacitive-comb transduced μresonator to –2 ppm/°C [11], at the cost of a more complex micromachining process.

4. Micromechanical Filters

The measured spectrum of Fig. 4 represents the frequency characteristic for a second-order, single-pole, bandpass filter centered at 16.5 kHz. Although useful for some applications, such as pilot tone filtering in mobile phones, second-order filter characteristics are generally inadequate for the majority of communications applications. Rather, bandpass filters

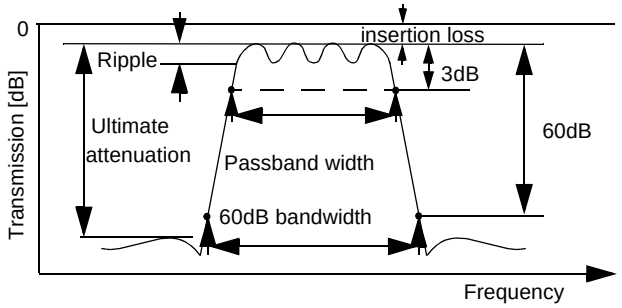

Fig. 10: Parameters typically used for filter specification.

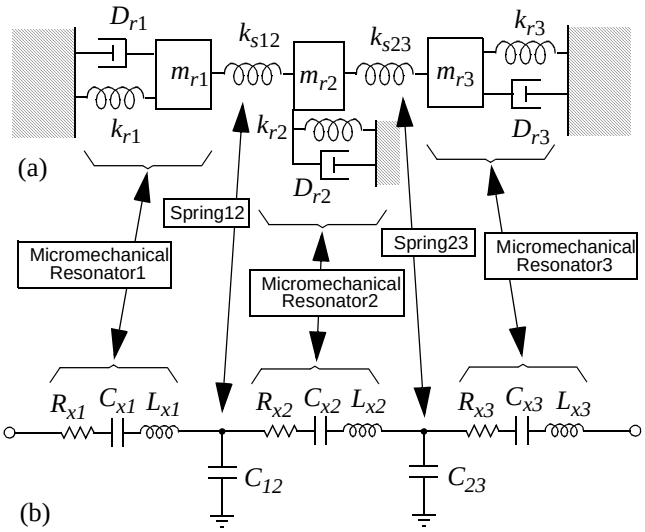

Fig. 11: (a) Equivalent lumped parameter mechanical circuit for a mechanical filter. (c) Corresponding equivalent LCR network.

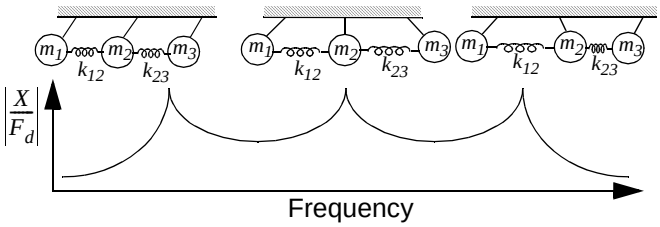

Fig. 12: Mode shapes of a three-resonator micromechanical filter and their corresponding frequency peaks.

such as depicted generically in Fig. 10 are required, with flatter passbands, sharper roll-offs, and greater stopband rejections.

General Mechanical Filter Design Concepts

To achieve the characteristic of Fig. 10, a number of micromechanical resonators are coupled together by soft coupling springs [24], as illustrated schematically in Fig. 11(a) using ideal mass-spring-damper elements. By linking resonators together using (ideally) massless springs, a coupled resonator system is achieved that now exhibits several modes of vibration. As illustrated in Fig. 12 for the coupled three-resonator system of Fig. 11, the frequency of each vibration mode corresponds to a distinct peak in the force-to-displacement frequency characteristic, and to a distinct, physical mode shape of the coupled mechanical resonator system. In the lowest

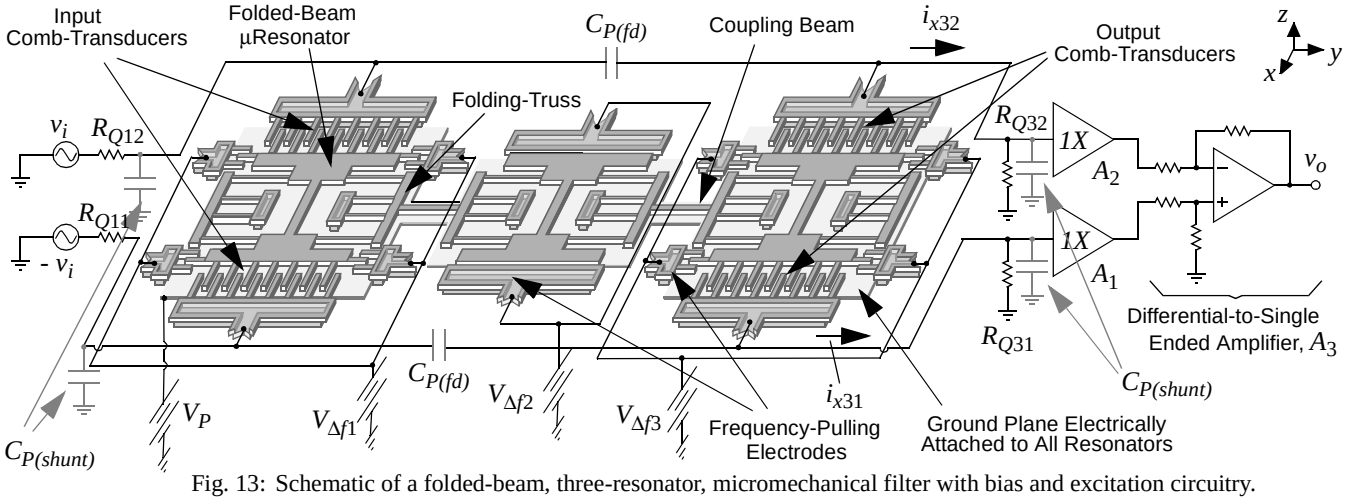

Fig. 13: Schematic of a folded-beam, three-resonator, micromechanical filter with bias and excitation circuitry.

frequency mode, all resonators vibrate in phase; in the middle frequency mode, the center resonator ideally remains motionless, while the end resonators vibrate 180° out of phase; and finally, in the highest frequency mode, each resonator is phase-shifted 180° from its adjacent neighbor. Without additional electronics, the complete mechanical filter exhibits the jagged passband seen in Fig. 12. As will be shown, termination resistors designed to lower the *Q*'s of the input and output resonators by specific amounts are required to flatten the passband and achieve a more recognizable filter characteristic, such as in Fig. 10

In practical implementations, because planar IC processes typically exhibit substantially better *matching* tolerances than *absolute*, the constituent resonators in μmechanical filters are normally designed to be identical, with identical spring dimensions and resonance frequencies. For such designs, the center frequency of the overall filter is equal to the resonance frequency f_o of the resonators, while the filter passband (i.e., the bandwidth) is determined by the spacings between the mode peaks.

The relative placement of the vibration peaks in the frequency characteristic—and thus, the passband of the eventual filter—is determined primarily by the stiffnesses of the coupling springs (k_{sij}) and of the constituent resonators (k_r). In particular, for a filter with center frequency f_o and bandwidth *BW*, these stiffnesses must satisfy the expression

$$BW = \left(\frac{f_o}{k_{ij}}\right)\left(\frac{k_{sij}}{k_r}\right) \tag{6}$$

where k_{ij} is a normalized coupling coefficient found in filter cookbooks [25]. Note from (6) that filter bandwidth is not dependent on the absolute values of resonator and coupling beam stiffness; rather, their ratio k_{sij}/k_r dictates bandwidth. Thus, the procedure for designing a mechanical filter involves two main steps: first, design of a mechanical resonator with resonance frequency f_o and reasonable stiffness k_r; and second, design of coupling springs with appropriate values of stiffness k_{sij} to achieve a desired bandwidth.

To take advantage of the maturity of LC ladder filter synthesis techniques, the enormous database governing LC ladder filter implementations [25], and the wide availability of electrical circuit simulators, realization of the μmechanical filter of Fig. 11(a) often also involves the design of an LC ladder version to fit the desired specification. The elements in the LC ladder design are then matched to lumped mechanical equivalents via electromechanical analogy, where inductance, capacitance, and resistance in the electrical domain equate to mass, compliance, and damping, respectively, in the mechanical domain. Figure 11(b) explicitly depicts the equivalence between the filter's lumped mass-spring-damper circuit and its electrical equivalent circuit. As shown, for this particular electromechanical analogy (the current analogy), each constituent resonator corresponds to a series LCR tank, while each (massless) coupling spring ideally corresponds to a shunt capacitor, with the whole coupled network corresponding to an LC ladder bandpass filter.

A Three-Resonator MF Micromechanical Filter

Figure 13 shows the perspective-view schematic of a practical three-resonator micromechanical filter [14,16]. As shown, this filter is comprised of three folded-beam μmechanical resonators mechanically coupled at their folding-trusses by soft, flexural-mode springs. The end resonators, which provide the filter inputs and outputs, feature capacitive-comb-transducers for enhanced linearity. In addition, these resonators, as well as the center resonator, are equipped with parallel-plate-capacitive transducers capable of tuning their frequencies [14]. The entire μmechanical filter structure, including resonators and coupling springs, is constructed of doped (conductive) polycrystalline silicon, and is suspended 2 μm over a uniform, doped-polysilicon ground plane that underlies the suspended structure at all points. This ground plane is required to prevent electrostatic pull-in of the structure into substrate, which can occur for structure-to-substrate voltage differences greater than 68 V.

To operate this filter, a dc-bias V_P is applied to the suspended, movable structure, while differential ac signals, v_i and $-v_i$, are applied through *Q*-controlling input resistors R_{Q11} and R_{Q12} to opposing ports of the input resonator, as shown in Fig. 13. The differential inputs applied to symmetrically opposing ports generate push-pull electrostatic forces on the input resonator, inducing mechanical vibration when the frequency of the input voltage comes within the passband of the mechanical filter. This vibrational energy is imparted to the center and output resonators via the coupling springs, causing them to vibrate as well. Vibration of the output reso-

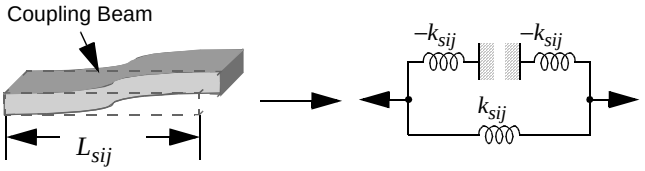

Fig. 14: Equivalent mechanical circuit for a quarter-wavelength flexural-mode coupling beam.

nator creates dc-biased, time-varying capacitors between the resonator and respective port electrodes, which source output currents given by

$$i_{xin} = V_{Pin}\frac{\partial C_{in}}{\partial x}\frac{\partial x}{\partial t}, \tag{7}$$

where x is displacement (defined in Fig. 13), C_{in} is the resonator-to-electrode capacitance at port n of resonator i, and V_{Pin} is the dc-bias voltage applied across C_{in}.

As shown in Fig. 13, the differential output currents i_{x31} and i_{x32} are directed through output Q-controlling resistors R_{Q31} and R_{Q32} forming voltages across these resistors which are sensed by buffers A_1 and A_2, then directed to the differential-to-single-ended converter A_3.

Quarter-Wavelength Coupling Beam Design—The equivalent mechanical circuit shown in Fig. 11(a) models an ideal case, where the springs coupling the resonators are massless. In reality, the coupling springs have finite mass that, without special design precautions, can add to adjacent resonators, shifting their frequencies and causing distortion of the filter passband. As described in [14], in order to accommodate this finite coupling beam mass while retaining the use of identical resonators in a μmechanical filter, the dimensions of the coupling beams must correspond to an effective quarter-wavelength of the operation frequency. Specifically, for quarter-wavelength coupling, the length L_{sij}, width W_{sij} and thickness h of a flexural-mode coupling beam must be chosen to simultaneously satisfy the expressions [14]

$$\cos\alpha\sinh\alpha + \sin\alpha\cosh\alpha = 0 \tag{8}$$

$$k_{sij} = -\frac{EI_s\alpha^3(\sin\alpha + \sinh\alpha)}{L_{sij}^3(\cos\alpha\cosh\alpha - 1)} \tag{9}$$

where $\alpha = L_{sij}(\rho A\omega_o{}^2/E/I_s)^{0.25}$, $I_s = hW_{sij}{}^3/12$, and $A = W_{sij}h$.

The equivalent mechanical circuit for a quarter wavelength coupling beam is massless, consisting of a network of positive- and negative-valued springs with equal magnitudes, as shown in Fig. 14. Given this, the equivalent mechanical and simplified electrical (using the current analogy) circuits for a three-resonator micromechanical filter using quarter-wavelength coupling springs is shown in Fig. 15, where quarter-wavelength couplers in the electrical domain are seen to consist of capacitive T-networks. The electrical equivalent circuit in Fig. 15 is somewhat simplified in that it does not precisely model the multi-port nature of the input and output resonators in a practical filter. For more precise modelling, multi-port equivalent circuits such as shown in Fig. 6 are required for the end resonators.

For a given value of film thickness h, and a given needed value of coupling beam stiffness k_{sij}, (8) and (9) represent two equations in two unknowns, implying that only one

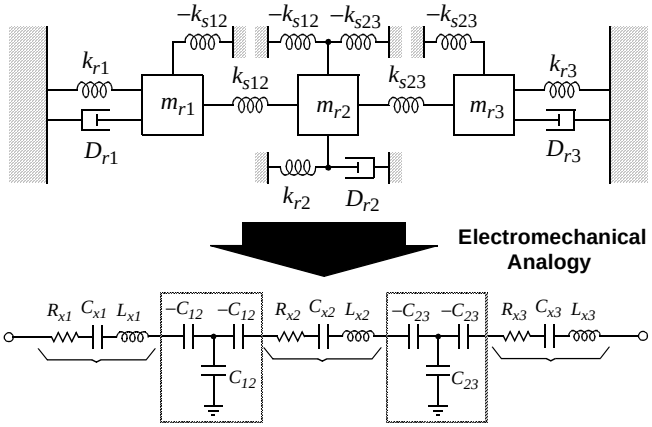

Fig. 15: Mechanical and (current analogy) electrical equivalent circuits for a quarter-wavelength coupled three-resonator micromechanical filter.

Table 3: Coupling Beam Width Requirements*

Percent *BW*	0.01%	0.1%	0.67%	1%
Req'd W_{sij} [μm]	0.06	0.28	1	1.32

*For a 455 kHz filter with k_r=310 N/m.

value of L_{sij} and one value of W_{sij} can be used to implement a given stiffness k_{sij}. If the resonator stiffness is further constrained to be constant—as was the case for the design in [14]—a scenario could arise where the unique coupling beam width W_{sij} that satisfies both quarter-wavelength and filter bandwidth requirements is a submicron dimension. Table 3 illustrates this problem for the case of a 455 kHz three-resonator filter with resonator stiffnesses constrained to be k_r=310 N/m (stiffness at the shuttle mass). Here, submicron dimensions are shown to be necessary for percent bandwidths (BW/f_o) lower than 0.67%.

Low-Velocity Coupling—To increase the required width of a quarter-wavelength coupling beam, the value of coupling beam stiffness k_{sij} corresponding to the needed filter bandwidth BW must be increased. As indicated by Eq. (6), for a given filter bandwidth, an increase in k_{sij} is allowable only when accompanied by an equal increase in resonator stiffness k_r. Such an increase in k_r must, in turn, be accompanied by a corresponding increase in resonator mass m_r to maintain the desired filter center frequency. Thus, to maximize flexibility in attainable filter bandwidth, a convenient method for simultaneously scaling both resonator stiffness k_r and mass m_r, preferably without drastically changing overall resonator dimensions, is required.

One simple method for achieving this takes advantage of the fact that, in general, the effective dynamic stiffness and mass of a given resonator are strong functions of location on the resonator, as illustrated in Fig. 16 for a classic folded-beam μmechanical resonator. This is immediately apparent with the recognition that different locations on a vibrating resonator move with different velocities, and that the dynamic mass and stiffness of a given mechanical resonator are strong functions of velocity, given by the expressions [24]

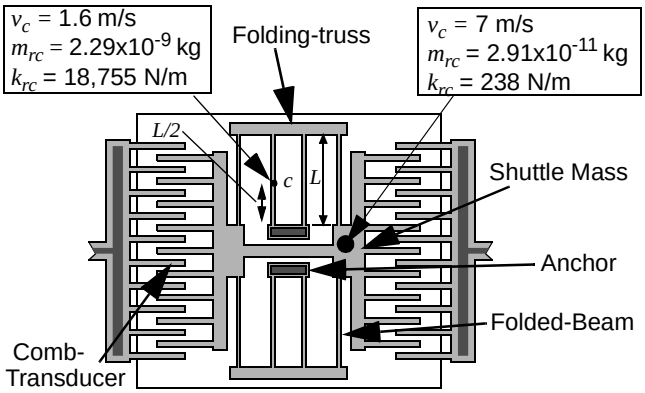

Fig. 16: Schematic of a classic folded-beam μresonator, indicating mechanical impedances at certain points.

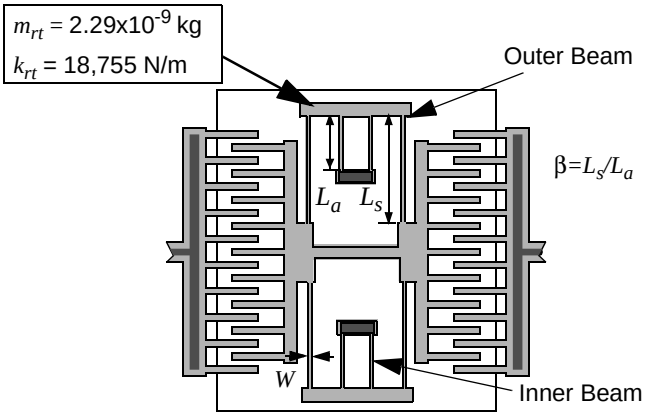

Fig. 17: Schematic of a ratioed folded-beam μresonator for low-velocity coupling applications.

$$m_{rc} = \frac{KE_{tot}}{(1/2)v_c^2} \tag{10}$$

$$k_{rc} = \omega_o{}^2 m_{rc}, \tag{11}$$

where KE_{tot} is the kinetic energy, ω_o is radian resonance frequency, and v_c is the resonance velocity magnitude at location c on the resonator. As a result, the dynamic resonator mass and stiffness "seen" by a coupling beam is a strong function of the coupling location. Fundamental-mode folded-beam resonators coupled at their shuttle masses, where the velocity magnitude is maximum, present the smallest stiffness to the coupling beam. Conversely, fundamental-mode resonators coupled at locations closer to their anchors, where velocities are many times smaller, present very large dynamic stiffnesses to their respective coupling beams, allowing much smaller percent bandwidth filters for the same coupling beam stiffnesses.

To conveniently implement low velocity coupling without substantial resonator design changes, and retaining coupling at resonator folding trusses, the folded-beam resonators used in Fig. 13 feature ratioed folded-beam lengths, as shown in Fig. 17. With this design, the resonance velocity magnitude of the folding truss can be varied according to

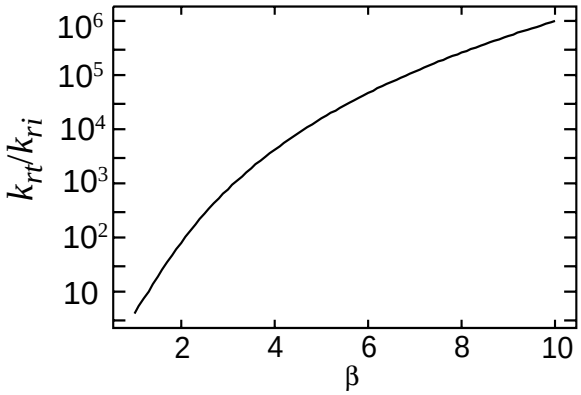

Fig. 18: Normalized effective stiffness at the folding-truss versus folded-beam ratio β.

$$v_{rt} = \frac{\omega_o X_0}{1+\beta^3} \tag{12}$$

where ω_o is the filter center frequency, X_o is the displacement magnitude at the shuttle mass, and β is the ratio of the outer beam length L_s to inner beam length L_a. Using (10) and (11), the effective dynamic stiffness k_{rt} and mass m_{rt} seen at the resonator folding trusses can be expressed as

$$k_{rt} = k_{ri}(1+\beta^3)^2 \tag{13}$$

$$m_{rt} = m_{ri}(1+\beta^3)^2 \tag{14}$$

where k_{ri} and m_{ri} are the effective dynamic stiffness and mass, respectively, at the resonator shuttle (maximum velocity point), given by

$$k_{ri} = \omega_o^2 m_{ri} \tag{15}$$

$$m_{ri} = M_p + \frac{M_t}{(1+\beta^3)^2} + \frac{13}{35(1+\beta^3)^2}M_{ba} + \left[\frac{1}{(1+\beta^3)} + \frac{13\beta^6}{35(1+\beta^3)^2}\right]M_{bs} \tag{16}$$

where

$$\omega_0 = \left[\frac{4Eh(W/L_a)^3}{(1+\beta^3)m_{ri}}\right]^{1/2}, \tag{17}$$

and where E is the Young's modulus; M_p is the mass of the shuttle; M_t, M_{ba}, and M_{bs} are the total folding truss, inner beam, and outer beam masses, respectively; h is thickness, and other dimensions are defined in Fig. 17.

Figure 18 plots the dynamic stiffness (normalized against effective stiffness at the shuttle mass) at the folding truss versus β, showing a full six orders of magnitude variation in stiffness for β's from 1 to 10. For a 360 kHz filter with 2 μm-width coupling beams, the stiffness variation shown in Fig. 18 corresponds to a range of percent bandwidths from 0.69% to 3×10^{-6}%.

Micromechanical Filter Termination—As mentioned previously, without the termination resistors R_{Qin} shown in Fig. 13, the passband of the μmechanical filter would be as shown in Fig. 12, comprised of three peaks, with excessive ripple. To obtain the designed value of passband ripple, the Q

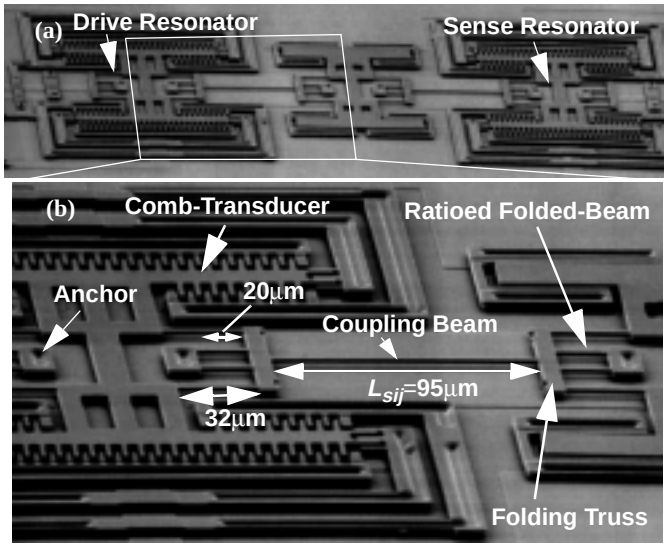

Fig. 19: SEM's of a fabricated ratioed folded-beam micromechanical filter. (a) Full view. (b) Enlarged partial view.

of the end resonators must be controlled to specific values dictated by filter synthesis or by cookbook tables [25]. For the design of Fig. 13, this is most easily done by placing resistors R_{Q1n} in series with each input and resistors R_{Q3n} in shunt with each output. The required resistor values are given by

$$R_{Qin} = \frac{1}{2}\left(\frac{Q_{res}}{q_i Q_{fltr}} - 1\right) R_{xin},\ i = 1, 3 \qquad (18)$$

where R_{xin} is defined in Fig. 6, Q_{res} is the initial, uncontrolled quality factor of the constituent resonators, Q_{fltr} is the quality factor of the overall filter ($Q_{fltr}=(f_o/BW)$), q_i is a normalized "q" value corresponding to the filter design in question (and easily found in filter cookbooks [25]), and n refers to a particular port of end resonator i.

The value of R_{Qin} greatly influences the magnitude of input-referred noise of the filter, as well as the degree of parasitic-induced passband distortion (caused by $C_{P(shunt)}$ and $C_{P(fd)}$ in Fig. 13). To minimize these effects, R_{Qin} must be minimized. From (18), this is best accomplished by minimizing the value of R_{xin}, which, with reference to Fig. 6, is in turn best accomplished by maximizing $\partial C_{in}/\partial x$, assuming that V_P is restricted by power supply limitations. $\partial C_{in}/\partial x$ is best maximized by minimizing the gap spacing between resonator and electrode comb fingers. Alternatively, if more transducer ports are available, active Q-control is also possible, which eliminates series resistors and offers both noise and dynamic range advantages [10].

MF Micromechanical Filter Performance—Wide-view and zoomed scanning electron micrographs (SEM's) for a polysilicon, surface-micromachined, low velocity-coupled, three-resonator μmechanical filter are presented in Fig. 19, with pointers to major components and key dimensions. The resonators in this filter are designed such that their folding truss resonance velocities are one-fifth the velocity at the shuttle (β=1.63). Since the shuttle moves faster than any other location on the resonator during resonance, the shuttle location corresponds to the maximum velocity point, and coupling at the folding trusses in this filter corresponds to one-fifth maximum velocity coupling. Design data for this filter, along with corresponding data for a half-maximum velocity coupled filter (β=1), are summarized in Table 4.

Table 4: MF Micromechanical Filter Design Summary

Parameter	Value		Units
Coupling Velocity, v_c	$v_{max}/2$	$v_{max}/5$	—
Folded-Beam Ratio, β	1	1.63	—
Designed Bandwidth, BW	1000	400	Hz
Measured Bandwidth, BW	757	403	Hz
Percent Bandwidth, (BW/f_o)	0.22	0.088	%
μRes. Folded-Beam Length, L_s	32.8	32.8	μm
μRes. Folded-Beam Length, L_a	32.8	20.1	μm
μRes. Folded-Beam Width, W_r	2	2	μm
Structural Layer Thickness, h	2	2	μm
Resonator Mass @ y_c, m_{rc}	$1\text{x}10^{-10}$	$8\text{x}10^{-10}$	kg
Resonator Stiffness @ y_c, k_r	1,239	6,618	N/m
Comb-Finger Gap Spacing, d	1	1	μm
Comb-Finger Overlap, L_o	5	5	μm
Coupling Beam Length, $L_{s12}=L_{s23}$	74	95	μm
Coupling Beam Width, $W_{s12}=W_{s23}$	1.2	2	μm
Coupling Beam Stiffness, $k_{s12}=k_{s23}$	1.76	3.76	N/m
Young's Modulus, E	150	150	GPa
Density of Polysilicon, ρ	2300	2300	kg/m^3
Filter DC-Bias, V_P	150	150	V
Q-Control Resistors, $R_{Q1n}=R_{Q2n}$	470	550	kΩ

Figures 20(a) and 20(b) compare transmission spectra for the half- (β=1) and one-fifth-maximum velocity (β=1.63) coupled μmechanical filters, respectively. As indicated in Table 4, even though the filter with half-maximum velocity coupling utilizes more compliant 1 μm-wide coupling beams, this filter still exhibits a larger bandwidth (757 Hz, Q_{fltr}=459) than its fifth-maximum velocity coupled counterpart, which uses stiffer 2 μm-wide coupling beams, yet achieves a bandwidth of only 403 Hz (Q_{fltr}=813). Furthermore, note from Table 4 that the fifth-velocity coupled filter was able to closely match the target bandwidth (within 0.75%), unlike its half-velocity counterpart, which missed its target by 24.3%. This result can be attributed to the wider coupling beams of the lower-velocity coupled filter, which are less susceptible to overetch-derived process variations than are the thinner beams of the higher-velocity coupled one. Decreased process susceptibility is, thus, a major advantage afforded by low-velocity coupling strategies.

It is noteworthy to mention that the measured data in Figs. 20(a) and 20(b) illustrate not only the effectiveness of low-velocity design techniques in achieving smaller percent bandwidths with improved accuracy, but also the impressive frequency response performance of μmechanical filters in general. In particular, Fig. 20(b) shows a filter response with

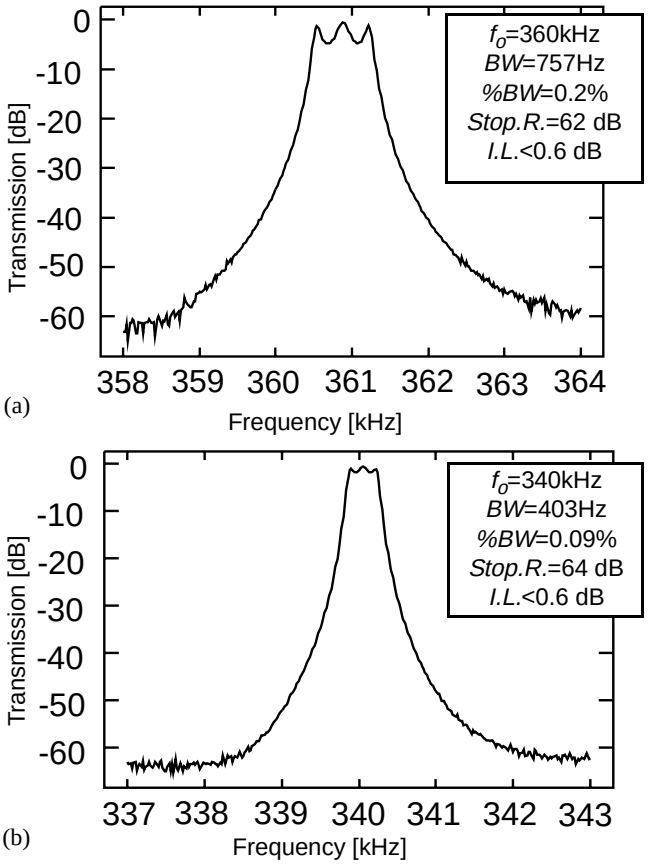

Fig. 20: Measured frequency spectra for low-velocity coupled, folded-beam MF filters. (a) Half-maximum velocity coupled. (b) One-fifth-maximum velocity coupled.

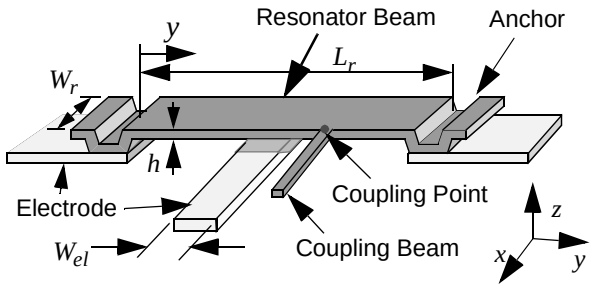

Fig. 21: Clamped-clamped beam μresonator.

a *Q* of 813, stopband rejection in excess of 64 dB, and an insertion loss of only 0.6 dB. Such performance rivals that of many macroscopic high-*Q* filters, including crystal filters, which are some of the best available.

A Two-Resonator HF Micromechanical Filter

As explained in [13], given the general expression for mechanical resonance frequency $\omega_o=(k_r/m_r)^{0.5}$, high frequency filters require resonators with much smaller mass. As a result, the folded-beam resonators used in the filter of Fig. 13 are inappropriate for HF or higher frequencies. Rather, clamped-clamped beam resonators, such as shown in Fig. 21, are more appropriate. Furthermore, as indicated in Table 4, some rather large voltages were required to achieve adequate electromechanical coupling via the comb-transducers shown in Fig. 13. To achieve more practical operation voltages, more efficient transducers are needed.

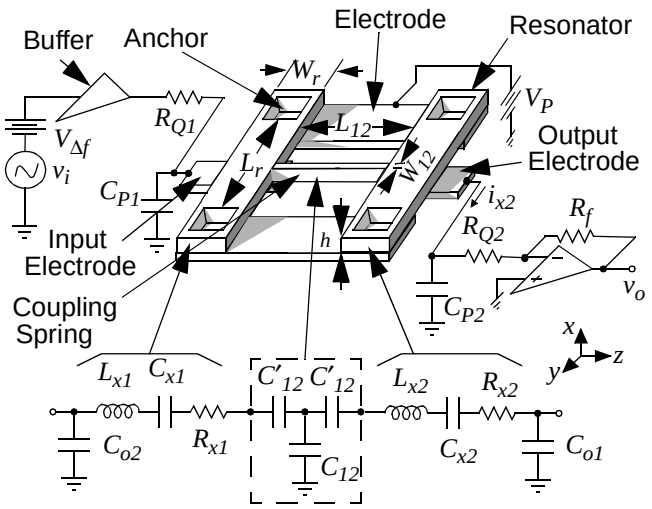

Fig. 22: Perspective view schematic of a two-resonator μmechanical filter, along with the preferred bias, excitation, and sensing circuitry, and the equivalent circuit for the filter.

HF Filter Structure and Operation—Figure 22 presents the perspective view schematic of a two-resonator, HF micromechanical filter, along with the preferred bias, excitation, and sensing circuitry. As shown, the filter consists of two μmechanical clamped-clamped beam resonators, coupled mechanically by a soft spring, all suspended 0.1 μm above the substrate. Conductive (polysilicon) strips underlie the central regions of each resonator and serve as capacitive transducer electrodes positioned to induce resonator vibration in a direction perpendicular to the substrate. The resonator-to-electrode gaps are determined by the thickness of a sacrificial oxide spacer during fabrication and can thus be made quite small (e.g., 0.1 μm or less), to maximize electromechanical coupling.

Under normal operation, the device is excited capacitively by a signal voltage applied to the input electrode. The output is taken at the other end of the structure, also via capacitive transduction. Upon application of an input with suitable frequency, the constituent resonators begin to vibrate in one or more flexural modes in a direction perpendicular to the substrate. For a properly designed mechanical filter, if the excitation voltage has a frequency within the passband, both resonators will vibrate. Vibration of the output resonator then couples to the output electrode, providing an output current i_{x2} given by an equation similar to (2), with *x* now representing displacement perpendicular to the substrate. The current i_{x2} is then directed to resistor R_{Q2}, which provides the proper termination impedance for the μmechanical filter. R_{Q2} then feeds a transresistance amplifier which amplifies i_{x2} to a buffered output voltage v_o. (Alternatively, a shunt resistor/buffer combination can be used, similar to that in Fig. 13.)

HF Filter Design—As with the previous filter, if each μresonator is made identical, the filter center frequency is determined primarily by the frequency of the constituent resonators. For the parallel-plate capacitively transduced

clamped-clamped beam resonators shown in Fig. 22, the resonance frequency is given by

$$f_o = 1.03\gamma\sqrt{\frac{E}{\rho}}\frac{h}{L_r^2}\left(1-\frac{k_e}{k_m}\right)^{1/2}, \quad (19)$$

where (approximately, neglecting the beam mode shape)

$$k_e = V_{Pn}^2\frac{C_{on}}{d^2}, \quad (20)$$

E and ρ are the Young's modulus and density of the structural material, respectively, h and L_r are specified in Fig. 22, k_m is the effective mechanical spring stiffness at the location in question, and γ is a scaling factor that models the effects of surface topography. For the μresonators of this work, γ is dominated by anchor step-up effects [26], which are predictable using finite element analysis. In practice, assuming a set value for V_P, designing for a specific frequency amounts to setting geometric dimensions L_r, W_r, and W_{el} via CAD layout, since all other variables are determined at the outset by fabrication technology.

Note from (19) that the resonance frequency of this device is tunable via adjustment of the dc-bias voltage V_P, and this can be used advantageously to implement filters with tunable center frequencies, or to correct for passband distortion caused by finite planar fabrication tolerances. The dc-bias dependence of resonance frequency arises from a V_P-dependent electrical spring constant k_e that subtracts from the mechanical spring constant of the system k_m, lowering the overall spring stiffness $k_r=k_m-k_e$, thus, lowering the resonance frequency [27]. This electrical spring constant k_e is generated by the nonlinear dependence of electrode-to-resonator gap capacitance $C(x)$ on displacement x, and as shown in (20), is proportional to the square of a (V_{Pn}/d) ratio, where V_n is the voltage on the electrode at port n (for multi-port resonators), $V_{Pn}=V_P-V_n$, and d is the electrode-to-resonator gap spacing.

The design procedure for HF micromechanical filters is virtually identical to that for the previous MF filters, differing only in the specific equations used. Electromechanical analogies are again utilized to design this filter, the bandwidth is again dictated by Eq. (6), and again, quarter-wavelength coupling beams and low-velocity coupling are utilized to achieve small percent bandwidths accurately. For clamped-clamped beam resonators, low velocity coupling is very easily achieved by merely moving the coupling location away from the center of the beam, as shown in Fig. 21. Using a procedure similar to that used to obtain (13) and (14), expressions for dynamic stiffness and mass as a function of distance y from an anchor are derived to be

$$k_r(y) = \omega_o^{\,2} m_r(y) \quad (21)$$

$$m_r(y) = \frac{\rho W_r h\int_0^{\sim r}[X(y')]^2 dy'}{[X(y)]^2}, \quad (22)$$

where

$$X(y) = (\cos ky - \cosh ky) - \sigma_n(\sin ky - \sinh ky), \quad (23)$$

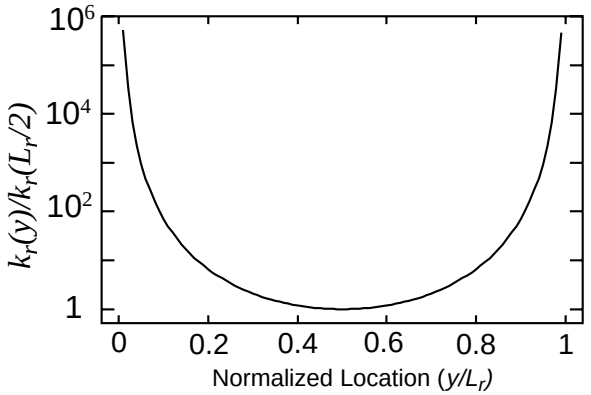

Fig. 23: Normalized effective stiffness versus normalized location on the resonator beam.

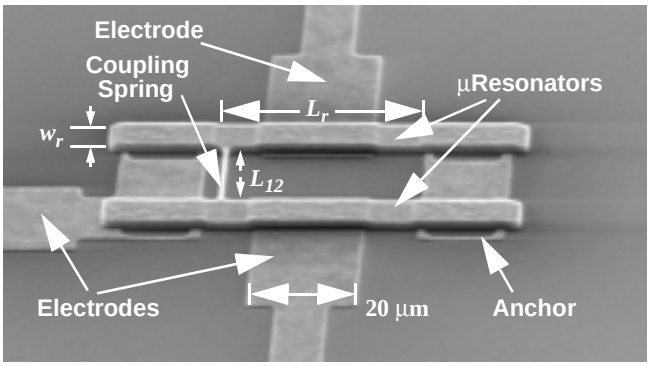

Fig. 24: SEM of a spring-coupled HF bandpass μmechanical filter and its measured frequency response spectrum.

and where ρ is the density of the structure material, $k = 4.73/L_r$ and σ_n=0.9825 for the fundamental mode, and dimensions are indicated in Fig. 21.

Figure 23 plots stiffness (normalized against the stiffness at the center of the resonator beam) versus normalized distance from an anchor for an ideal clamped-clamped beam resonator, indicating a six order of magnitude variation in stiffness for coupling locations $L_r/10$ to $L_r/2$ distant from the anchor. For a 10 MHz filter using 2 μm-wide coupling beams, this corresponds to a range of percent bandwidths from 0.33% to 24%.

HF Micromechanical Filter Performance—The SEM for an 8.5 MHz, two-resonator, low-velocity coupled micromechanical filter constructed of phosphorous-doped polysilicon is shown in Fig. 24. Design details for this filter are summarized in Table 5, along with operation voltages and Q-controlling resistor values. Note from the table that due to the use of small electrode-to-resonator gap spacings, a dc-bias voltage V_P much smaller than required for the previous comb-driven filter can now be used, and Q-controlling termination resistors are now on the order of only 4.4 kΩ. With even smaller gaps, lower values of V_P and R_Q are expected. For example, an electrode-to-resonator gap spacing of 200 Å would allow the use of a 4 V dc-bias with 134 Ω termination resistors.

The measured transmission spectrum for this filter is presented in Fig. 25. As shown, a percent bandwidth of 0.2% was achieved with an associated insertion loss of less than 1

Table 5: HF μMechanical Filter Data

Parameter	Value	Units
μResonator Beam Length, L_r	40.8	μm
μResonator Beam Width, W_r	8	μm
Structural Layer Thickness, h	2	μm
μResonator Effective Mass, m_{ri}	7.05×10^{-13}	kg
μResonator Spring Constant, k_{ri}	1,950	N/m
Electrode-to-Resonator Overlap	160	μm^2
Electrode-to-Resonator Gap, d	0.1	μm
$\partial C_n/\partial x = C_{on}/d$	$1.4\text{x}10^{-7}$	F/m
Coupling Beam Length, L_{12}	20.35	μm
Coupling Beam Width, W_{12}	0.75	μm
Q_{fltr} at $L_{coup}= L_r/10$ (calculated)*	368	—
Q_{fltr} at $L_{coup}= L_r/10$ (measured)*	341	—
Q_{fltr} at $L_{coup}= L_r/2$ (calculated)*	11	—
Q_{fltr} at $L_{coup}= L_r/2$ (measured)*	24	—
Dc-bias Voltage, V_P	20	V
Termination Resistors (for $L_r/10$), R_{Qn}	4.4	kΩ

*L_{coup}= distance from the anchor to where the coupler attaches to the resonator beam

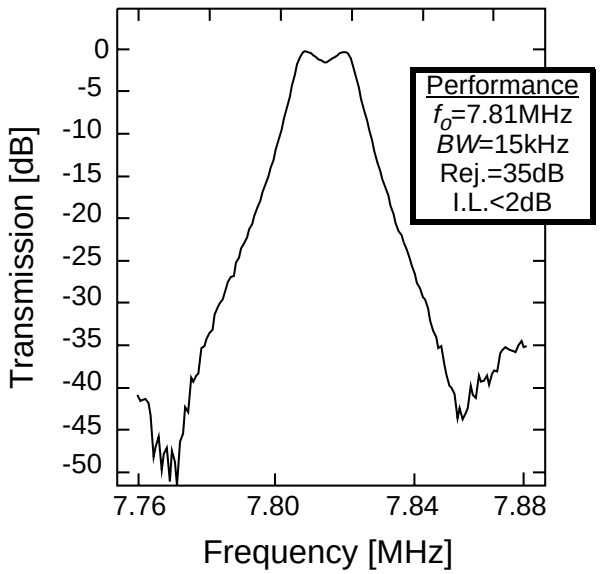

Fig. 25: Measured transmission spectrum for an HF two-resonator micromechanical filter, such as shown in Fig. 24.

dB, and a stopband rejection exceeding 35 dB. Again, these are impressive figures for a two-resonator bandpass filter, clearly indicative of the use of high-Q resonators.

5. Frequency Range Of Applicability

The ultimate frequency range of the described micromechanical resonators is of great interest and is presently a topic under intense study. From a purely geometric standpoint, the frequency range of micromechanical resonators can extend

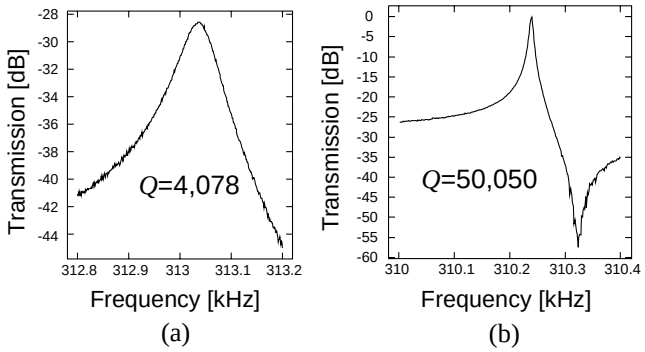

Fig. 26: Measured transconductance spectra for (a) a $POCl_3$-doped resonator and (b) an implant-doped version, both after furnace annealing.

well into the gigaHertz range. For example, the dimensions of a clamped-clamped beam resonator required to attain a frequency of 1 GHz are (referring to Fig. 1) approximately $L\approx4$ μm, W=2 μm, and h=2 μm, where finite-element analysis should be used to account for width and anchoring effects. This frequency can also be attained by longer beams vibrating in higher modes. Thus, according to analytical and finite element prediction, frequencies into the gigaHertz range are geometrically possible.

Geometry, however, is only one of many important considerations. The applicable frequency range of micromechanical resonators will also be a function of several other factors, including:

(1) quality factor, which may change with frequency for a given material, depending upon frequency-dependent energy loss mechanisms [28];

(2) series motional resistance R_x (c.f., Fig. 22), which must be minimized to suppress input-referred noise and alleviate filter passband distortion due to parasitics [13,14,15];

(3) absolute and matching tolerances of resonance frequencies, which will both be functions of the fabrication technology and of frequency trimming or tuning strategies [29]; and

(4) stability of the resonance frequency against temperature variations, mass loading, aging, and other environmental phenomena.

Each of the above phenomena are currently under study. In particular, assuming adequate vacuum can be achieved, the ultimate quality factor will be strongly dependent upon the material type, and even the manufacturing process. For example, surface roughness or surface damage during fabrication may play a role in limiting quality factor. In fact, preliminary results comparing the quality factor achievable in diffusion-doped polysilicon structures (which exhibit substantial pitting of the poly surface) versus implant-doped ones, indicate that the latter exhibit almost an order of magnitude higher Q at frequencies near 10 MHz. Figure 26 presents measured transconductance spectra for two comb-driven folded-beam micromechanical resonators fabricated in the same polycrystalline material, but doped differently—one $POCl_3$-doped, the other phosphorous implant-doped—using the process sequences summarized in Table 6 [29]. The difference in Q is very intriguing, and is consistent with a surface roughness-dependent dissipation mechanism.

Table 6: Doping Recipes

$POCl_3$	Implant
(v) Deposit 2 μm LPCVD fine-grained polysilicon @ 588°C	(i) Deposit 1 μm LPCVD fine-grained polysilicon @ 588°C
(vi) Dope 2.5 hrs. @ 950°C in $POCl_3$ gas	(ii) Implant phosphorous: Dose=10^{16} cm^{-2}, Energy=90 keV
(vii) Anneal for 1 hr. @ 1100°C in N_2 ambient	(iii) Deposit 1 μm LPCVD fine-grained polysilicon @ 588°C
	(iv) Anneal for 1 hr. @ 1100°C in N_2 ambient

From a design perspective, one loss mechanism that may become more important with increasing frequency is loss to the substrate through anchors. Anti-symmetric resonance designs, such as balanced tuning forks, could prove effective in alleviating this source of energy loss.

Electromechanical Coupling

In addition to possible Q limitations, the practical frequency range of micromechanical resonators is limited by electromechanical coupling, which is largest when the series motional resistance R_x is smallest. R_x, indicated in Fig. 6, is given by the expression [17]

$$R_x = \frac{\sqrt{k_r m_r}}{Q V_P^2 (\partial C/\partial x)^2}, \tag{24}$$

where k_r is the system spring constant, and m_r is the effective mass of the resonator. Given that a frequency increase on this micro-scale entails an increase in k_r with only a slight decrease in mass m_r, (24) suggests that R_x increases gradually with frequency. For a given frequency, R_x may be reduced by increasing the dc-bias V_P or the $\partial C/\partial x$ term. The value to which V_P may be raised is limited by the available supply voltage, or by the maximum voltage obtainable through charge-pumping. The $\partial C/\partial x$ term is proportional to the electrode-to-resonator overlap area and inversely proportional to the electrode-to-resonator gap spacing. The overlap area is limited by width effects on the resonance frequency, while the gap spacing is limited by technology. For the HF filter described above, the gap spacing is defined by an oxide spacer thickness, and thus, can be made very small, on the order of tens to hundreds of Angstroms. For this reason, the minimum gap spacing is likely not determined by process limitations, but rather by dynamic range considerations.

Dynamic Range

The dynamic range in the passband of a μmechanical filter can be determined through consideration of nonlinearity in its electromechanical transducers and noise produced by its termination resistors. For the purposes of deriving an expression for filter dynamic range in the passband, Fig. 27 presents the equivalent circuit for an n-resonator filter for input frequencies within the passband.

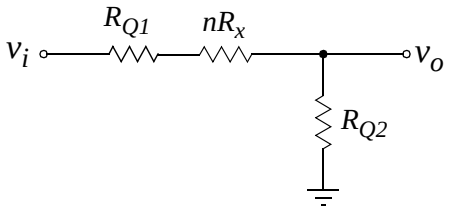

Fig. 27: Equivalent circuit for an n-resonator micromechanical filter for input frequencies within the passband.

Dynamic range in the filter passband is defined by the ratio of the maximum input power v_{imax}^2 (determined by nonlinearity) to the minimum detectable signal $\overline{v_n^2}$ (determined by input-referred noise); i.e.,

$$DR = \frac{v_{imax}^2}{\overline{v_n^2}}. \tag{25}$$

The total input-referred noise power in this passive system is comprised primarily of thermal noise from the termination resistors R_{Q1} and R_{Q2}, plus small contributions from the resonator R_x's, which actually represent Brownian motion noise of the constituent resonators. An expression for the total input-referred noise power is then given by

$$\overline{v_n^2} = 4k_B T(2R_Q + nR_x)\Delta f \approx 4k_B T(2R_Q)\Delta f, \tag{26}$$

where k_B is Boltzmann's constant, T is temperature, it has been assumed that R_{Q1}=R_{Q2}=R_Q, and the last equation holds for filters with low insertion loss (i.e., $R_Q >> R_x$).

The maximum input voltage v_{imax} is determined by the maximum allowable displacement that maintains adequate transducer linearity or resonator stiffness linearity. If displacements x are assumed small enough that stiffness nonlinearity is not an issue, then the maximum allowable input voltage with frequency in the filter passband is given approximately (neglecting beam mode shape) by

$$v_{imax} = \frac{2k_{ri}x_{max}}{q_i Q_{fltr} V_P (\partial C/\partial x)}, \tag{27}$$

where k_{ri} is the resonator stiffness at the location of the input electrode, and x_{max} is the maximum allowable displacement magnitude at the electrode location determined by nonlinear distortion.

Inserting (26) and the rms value of (27) into (25), an approximate expression for the dynamic range in the passband of the filter in Fig. 27 is

$$DR = 10\log\left[\frac{2\pi k_{ri} x_{max}^2}{4k_B T q_i}\right] \quad [\text{in dB}]. \tag{28}$$

For the case where clamped-clamped beam, parallel-plate capacitively transduced μmechanical resonators are used in the filter, (28) reduces to

$$DR = 10\log\left[\frac{2\pi k_{ri} a^2 d^2}{4k_B T q_i}\right] \quad [\text{in dB}], \tag{29}$$

where d is the electrode-to-resonator gap spacing at both input and output transducers, and a is a constant determined

by the magnitude of acceptable IM_3 distortion [30]. Note that *DR* decreases with gap spacing. On the other hand, input-referred noise, which is proportional to R_x, increases with gap spacing. Thus, for the filter design of Fig. 22 there is a trade-off between dynamic range and minimum detectable signal (*MDS*). Alternative μmechanical filter designs can be used to alleviate this situation. For example, design of the filter of Fig. 13 is influenced much less by this trade-off, because it utilizes capacitive-comb transducers, which are ideally linear over very large displacements. Due to their large mass, however, comb-transducers are less practical for high frequency designs. Furthermore, comb-capacitive transducers provide less electromechanical coupling than parallel-plate capacitive ones, so while they do enhance the overall dynamic range by virtue of their linearity, they do so at the cost of reduced *MDS*. Alternative linearization methods are the subject of current research.

6. Conclusions

Low-phase noise oscillators and high-*Q* filters utilizing micromechanical vibrating resonator tanks have been demonstrated with frequencies from the LF to HF range, and requiring areas of less than 0.005 mm^2 per device on average. From a purely geometrical standpoint, the described IC-compatible mechanical resonators should be able to achieve vibrational frequencies well into the gigaHertz range. However, considerations other than geometry, such as frequency-dependent loss mechanisms, electromechanical coupling, and matching tolerances, all of which affect the ultimate performance of the described oscillators and filters, will most likely dictate the ultimate frequency range of this technology. For the case of filters, dynamic range and minimum detectable signal are found to be competing attributes in some designs. The trade-offs, however, can be made much less severe with proper design techniques.

Acknowledgments

The author gratefully acknowledges substantial contributions from former and present graduate students, in particular Frank Bannon III and Kun Wang, who are responsible for the filter results.

References

[1] E. Frian, S. Meszaros, M. Chuaci, and J. Wight, "Computer-aided design of square spiral transformers and inductors," *1989 IEEE MTT-S Dig.*, pp. 661-664.

[2] N. M. Nguyen and R. G. Meyer, "Si IC-compatible inductors and *LC* passive filters," *IEEE J. of Solid-State Circuits*, vol. SC-25, no. 4, pp. 1028-1031, Aug. 1990.

[3] N. M. Nguyen and R. G. Meyer, "A 1.8-GHz monolithic *LC* voltage-controlled oscillator," *IEEE J. of Solid-State Circuits*, vol. SC-27, no. 3, pp. 444-450.

[4] S. V. Krishnaswamy, J. Rosenbaum, S. Horwitz, C. Yale, and R. A. Moore, "Compact FBAR filters offer low-loss performance," *Microwaves & RF*, pp. 127-136, Sept. 1991.

[5] R. Ruby and P. Merchant, "Micromachined thin film bulk acoustic resonators," *Proceedings* of the 1994 IEEE International Frequency Control Symposium, Boston, MA, June 1-3, 1994, pp. 135-138.

[6] A. A. Abidi, "Direct-conversion radio transceivers for digital communications," *IEEE J. Solid-State Circuits*, vol. 30, No. 12, pp. 1399-1410, Dec. 1995.

[7] D. H. Shen, C.-M. Hwang, B. B. Lusignan, and B. A. Wooley, "A 900-MHz RF front-end with integrated discrete-time filtering," *IEEE J. of Solid-State Circuits*, vol. 31, no. 12, pp. 1945-1954, Dec. 1996.

[8] W. C. Tang, T.-C. H. Nguyen, and R. T. Howe, "Laterally driven polysilicon resonant microstructures," *Sensors and Actuators*, **20**, 25-32, 1989.

[9] R. T. Howe and R. S. Muller, "Resonant microbridge vapor sensor," *IEEE Trans. Electron Device*s, ED-33, pp. 499-506, 1986.

[10] C. T.-C. Nguyen and R. T. Howe, "Quality factor control for micromechanical resonators," *Technical Digest*, IEEE International Electron Devices Meeting, San Francisco, California, December 14-16, 1992, pp. 505-508

[11] C. T.-C. Nguyen and R. T. Howe, "Microresonator frequency control and stabilization using an integrated micro oven," *Digest of Technical Papers*, the 7th International Conference on Solid-State Sensors and Actuators (Transducers'93), Yokohama, Japan, pp. 1040-1043, June 7-10, 1993.

[12] C. T.-C. Nguyen, "High-*Q* micromechanical oscillators and filters for communications (invited)," 1997 IEEE International Symposium on Circuits and Systems, Hong Kong, June 9-12, 1997, pp. 2825-2828.

[13] F. D. Bannon III and C. T.-C. Nguyen, "High frequency microelectromechanical IF filters," *Technical Digest*, 1996 IEEE Electron Devices Meeting, San Francisco, CA, Dec. 8-11, 1996, pp. 773-776.

[14] K. Wang and C. T.-C. Nguyen, "High-order micromechanical electronic filters," *Proceedings*, 1997 IEEE International Micro Electro Mechanical Systems Workshop, Nagoya, Japan, Jan. 26-30, 1997, pp. 25-30.

[15] J. R. Clark, A.-C. Wong, and C. T.-C. Nguyen, "Parallel-resonator HF Micromechanical Bandpass Filters," *Digest of Technical Papers*, 1997 International Conference on Solid-State Sensors and Actuators, Chicago, Illinois, June 16-19, 1997, pp. 1161-1164.

[16] K. Wang, J. R. Clark, and C. T.-C. Nguyen, "*Q*-enhancement of micromechanical filters via low-velocity spring coupling," to be published in the *Proceedings* of the 1997 IEEE International Ultrasonics Symposium, Toronto, Ontario, Canada, Oct. 5-8, 1997.

[17] C. T.-C. Nguyen and R. T. Howe, "An integrated CMOS micromechanical resonator high-*Q* oscillator," to be published in *IEEE Trans. Electron Devices*.

[18] C. T.-C. Nguyen and R. T. Howe, "Design and performance of monolithic CMOS micromechanical resonator oscillators," *Proceedings*, 1994 IEEE International Frequency Control Symposium, Boston, MA, May 31-June 3, 1994, pp. 127-134.

[19] C. T.-C. Nguyen and R. T. Howe, "CMOS Micromechanical Resonator Oscillator," *Technical Digest*, IEEE

International Electron Devices Meeting, Washington, D. C., pp. 199-202, December 5-8, 1993.

[20] T. A. Core, W. K. Tsang, S. J. Sherman, "Fabrication technology for an integrated surface-micromachined sensor," *Solid State Technology*, pp. 39-47, Oct. 1993.

[21] R. D. Nasby, J. J. Sniegowski, J. H. Smith, S. Montague, C. C. Barron, W. P. Eaton, P. J. McWhorter, D. L. Hetherington, C. A. Apblett, and J. G. Fleming, "Application of chemical-mechanical polishing to planarization of surface-micromachined devices," *Technical Digest*, 1996 Solid-State Sensor and Actuator Workshop, Hilton Head, South Carolina, pp. 48-53, June 3-6, 1996.

[22] J. M. Bustillo, G. K. Fedder, C. T.-C. Nguyen, and R. T. Howe, "Process technology for the modular integration of CMOS and polysilicon microstructures," *Microsystem Technologies*, **1** (1994), pp. 30-41.

[23] H. Guckel, *et al.*, "The mechanical properties of fine-grained polysilicon: the repeatability issue," Technical Digest, IEEE Solid-State Sensor and Actuator Workshop, Hilton Head Island, S. C., June 1988, pp. 96-99.

[24] R. A. Johnson, *Mechanical Filters in Electronics*, New York: John Wiley & Sons, 1983.

[25] A. I. Zverev, *Handbook of Filter Synthesis*, New York: John Wiley & Sons, 1967.

[26] Q. Meng, M. Mehregany, and R. L. Mullen, "Theoretical modelling of microfabricated beams with elastically restrained supports," J. Microelectromech. Syst., vol. 2, no. 3, pp. 128-137, Sept. 1993.

[27] H. Nathanson, W. E. Newell, R. A. Wickstrom, and J. R. Davis, Jr., "The resonant gate transistor," *IEEE Trans. Electron Devices*, vol. ED-14, No. 3, pp. 117-133, March 1967.

[28] V. B. Braginskky, V. P. Mitrofanov, and V. I. Panov, *Systems With Small Dissipation.* Chicago: University of Chicago Press., 1985.

[29] K. Wang, A.-C. Wong, W.-T. Hsu, and C. T.-C. Nguyen, "Frequency-trimming and *Q*-factor enhancement of micromechanical resonators via localized filament annealing," *Digest of Technical Papers*, 1997 International Conference on Solid-State Sensors and Actuators, Chicago, Illinois, June 16-19, 1997, pp. 109-112.

[30] C. T.-C. Nguyen, "Micromechanical Signal Processors," Ph.D. Dissertation, Dept. of Electrical Engineering and Computer Sciences, University of California at Berkeley, December 1994.

Clark T.-C. Nguyen *was born in Austin, Texas on March 29, 1967. He received the B. S., M. S., and Ph.D. degrees from the University of California at Berkeley in 1989, 1991, and 1994, respectively, all in Electrical Engineering and Computer Sciences.*

In 1995, he joined the faculty of the University of Michigan, Ann Arbor, where he is currently an Assistant Professor in the Department of Electrical Engineering and Computer Science. His research interests focus upon micro electromechanical systems, including integrated micromechanical signal processors and sensors, merged circuit/micromechanical technologies, RF communication architectures, and integrated circuit design and technology. Recent research results include the first fully monolithic high-Q oscillator and the first micromachined mechanical filters. Dr. Nguyen's research group at the University of Michigan is presently investigating extension of the frequency range of micromechanical signal processors (filters and oscillators) into the UHF range, developing merged circuit/microstructure technologies, studying physical phenomena that influence the frequency stability of micro- and nano-scale mechanical resonators, exploring novel architectures for single-chip transceivers for military and commercial applications using MEMS technologies, developing automatic generation codes for mechanical filter design, and designing and implementing novel, completely monolithic integrated sensors.

From 1995 to 1996, Dr. Nguyen has served as a member of NASA's New Millennium Integrated Product Development Team (IPDT) on Communications, which roadmaps future communications technologies for NASA use into the turn of the century. He is now a Consulting Member.